

Effect of Integration of Scramjet into Airframe on Engine Performance and Payload *

Daisuke AKIHISA^{*1} Takeshi KANDA^{*2} Kouichiro TANI^{*2}
Kenji KUDO^{*2} and Goro MASUYA^{*3}

ABSTRACT

There are three typical configurations for integrating the scramjet into the airframe of aerospace planes. They are (1) the whole engine is on the windward ramp surface of the airframe, (2) the engine is located downstream of the forebody ramp where the surface of the airframe is parallel to the airframe axis, and (3) the inlet entrance is on the ramp surface with the following engine parts parallel to the airframe axis. To examine the effect of the integrating forms on the engine performance, several types of the inlet models were tested in a wind tunnel, and simulations of the scramjet engine and the flight of the aerospace plane were conducted. The experimental results showed that the first and the third configurations showed better mass capture. In the second configuration, the pre-compression effect was neutralized by the expansion fan from the corner of the downstream end of the ramp. All configurations showed similar levels of kinetic energy efficiencies. The simulation based on the experimental results showed that the third configuration produced the best engine thrust and the least airframe drag. On the other hand, in the second configuration, the payload became negative. Thus, it is recommended that the inlet should be located on the windward ramp surface of the vehicle to inhale the pre-compressed air, and the following engine components should be parallel to the airframe axis to reduce the cowl drag and to increase the thrust at the external nozzle.

Keywords: scramjet, inlet, mass capture, aerospace plane

概 要

スクラムジェットのスペースプレーン機体への組込み方法には大別して以下の3とおりが挙げられる。(1)エンジン全体を機体下面の予圧縮面に取り付ける、(2)下流で機軸と平行になった機体下面にエンジンを取り付ける、(3)インレットは機体下面の予圧縮面に取付け、エンジン下流部は機軸と平行になった面に取り付ける。組込み方法がエンジン性能に与える影響について調べるために数種類のインレット模型をマッハ4風洞で試験し、その結果に基づきスクラムジェットエンジンの性能を計算し、スペースプレーンの飛行シミュレーションを行った。実験によって(1)および(3)の組込み状態で良好な空気捕獲率が得られた。(2)の形態では、機体下面での予圧縮効果がエンジン入口での膨張波によって打ち消された。どの形態でもほぼ同じ運動エネルギー効率が得られた。エンジン性能計算では(3)の形態での推力が最大で、最小の抗力となった。(2)の形態ではペイロードは負となった。エンジンの機体組込み方法としては、インレットは予圧縮面取付け、その下流のエンジン部はカウル抗力を減らして外部ノズル推力を増やすために機軸と平行とすべきであることが示された。

* received 9 January, 2002 (平成 14 年 1 月 9 日受付)

^{*1} Engineer, Higashi-fuji Technical Center, Toyota Motor Corporation, Susomo, Shizuoka 410-1193. Formerly Graduate Student of Tohoku University. (トヨタ自動車株式会社第四開発センター、前東北大学大学院)

^{*2} Ramjet Propulsion Research Center (ラムジェット推進研究センター)

^{*3} Professor, Department of Aeronautics and Space Engineering, Tohoku University, Aoba-ku, Sendai, Miyagi 980-8579 (東北大学工学部機械航空学科教授)

NOMENCLATURE

A	: area
C_F	: thrust coefficient
CR	: capture ratio
M	: Mach number
P	: pressure
α	: ramp angle or inclined angle of the top wall in the experiments
δ	: boundary layer thickness at 99% of the primary flow velocity
η	: efficiency
ξ	: ratio of averaged top wall pressure in isolator to free stream pressure

Subscripts

KE	: kinetic energy
P_t	: total pressure
all	: total thrust with windward-surface airframe drag, engine-thrust, and external-nozzle thrust
$inlet$: performance of inlet itself excluding the pre-compression effect
ref	: free-stream reference condition in the experiments, i.e., inclusion of a boundary layer on the plate and no inclination of top-wall plate
t	: stagnation condition
$total$: inlet performance with pre-compression effect
w	: wall
0	: wind tunnel reservoir condition
1	: at the inlet entrance
2	: in the isolator
∞	: free stream, flight condition

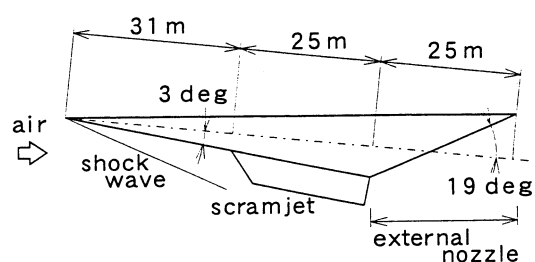
INTRODUCTION

A scramjet engine has high performance potential at hypersonic flight of aerospace planes and hypersonic aircrafts. Integration of the engine into the airframe is beneficial because the fore- and the aft-bodies of the vehicle perform as a pre-compression stage and an external expansion stage, respectively.¹⁾ In the airframe-engine integrated compression system, one or several oblique shock waves from the windward surface of the airframe are used for external compression. Several types of airframe-engine integration have been proposed and schematically illustrated in journal articles, technical papers and

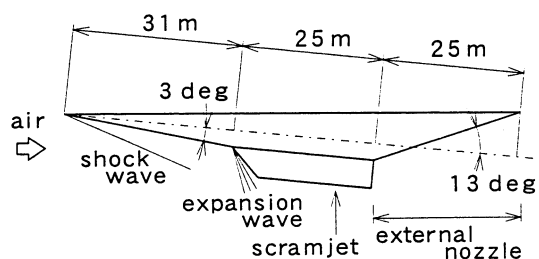
textbooks. They can be categorized into the following three configurations for engine mounting location.

(1) Type *a* (Fig. 1(a))

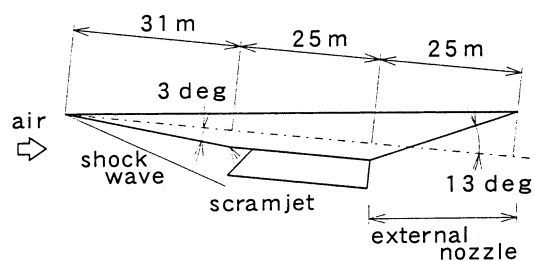
The entire engine is attached to the ramp of the airframe, and the side view of the undersurface of the airframe forms a triangle or a flat-plate.¹⁾⁻⁴⁾ In some cases, the engine is attached to the horizontal undersurface of the airframe, but with the attack angle, the undersurface practically works as a ramp. The airframe aft-surface downstream of the engine works as an external nozzle. The axis of the engine is straight.



(a) Side view of Type a. The engine is integrated on the ramp of the airframe.



(b) Side view of Type b. The engine is attached downstream of the rear corner of the airframe ramp.



(c) Side view of Type c. The inlet is located on the ramp, and the rest of the engine is parallel to the airframe axis.

Fig. 1 Vehicle configuration models for performance calculation.

(2) Type *b* (Fig. 1(b))

The side view of the undersurface of the airframe forms a trapezoid or a triangle. The engine is attached downstream of the ramp where the surface is parallel to the airframe-axis.⁵⁾⁻⁸⁾

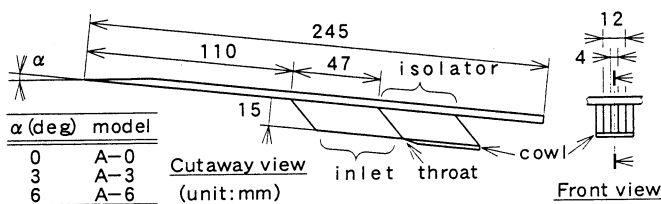
(3) Type *c* (Fig. 1(c))

The side view of the undersurface of the airframe forms also a trapezoid, and the engine straddles over the ramp and the parallel surface. The inlet is located on the ramp with the following engine parts parallel to the airframe axis.⁹⁾⁻¹²⁾

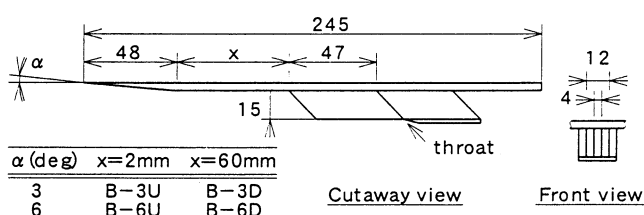
The airflow conditions at the entrance of the engine have been investigated with several airframe configurations,^{13),14)} but they were not related to the engine performance. The effect of the integration of the scramjet engine into the airframe on engine performance and on payload of the aerospace plane has not been discussed sufficiently. In the present study, airframe-integrated scramjet inlet models were experimentally investigated in a Mach 4 wind tunnel to obtain characteristics of the three types of the integration. Then, based on the experimental results, simulations of the scramjet engine and the flight of the Single-Stage-to-Orbit (SSTO) aerospace plane were conducted with simplified models to evaluate the influence of the integration form on the engine performance and the payload.

EXPERIMENTS OF INLET MODELS

The characteristics of each integration form were investigated in the experiments with the scramjet inlet



(a) Type A model



(b) Type B model

models. In Type *b* configuration, the expansion fan from the rear corner enters the inlet, and as a results, the flow field inside the inlet is highly distorted and unpredictable. Modeling of the inhaling of the expansion fan from the airframe-ramp was one of the major subjects of this testing.

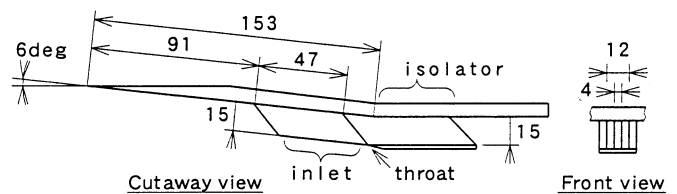
Experimental apparatus

(A) Wind tunnel

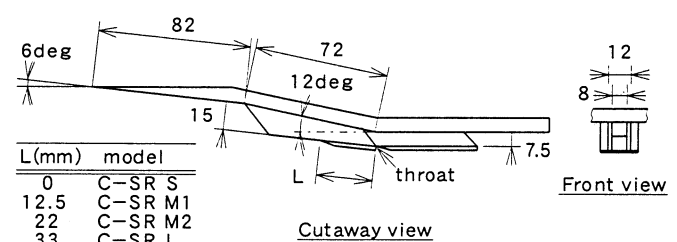
Experiments were conducted in a Mach 4 blow-down wind tunnel with a rectangular test section of 100 mm by 110 mm.¹⁵⁾ The total pressure and the total temperature were 2.2 MPa and 285K, respectively. The duration time of a test was 20 seconds, sufficiently long enough to measure multiple wall pressures with two mechanical pressure scanners (Scanivalves®). The unit Reynolds number was $1.2 \times 10^8 \text{ m}^{-1}$.

(B) Airframe-integrated inlet models

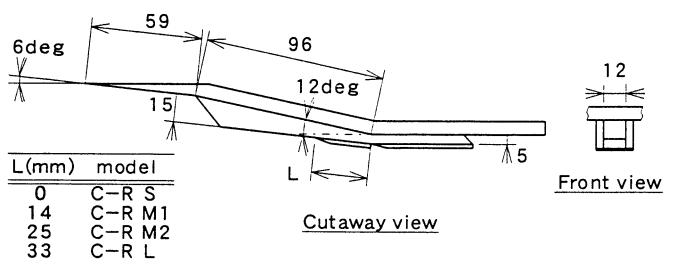
Figures 2 (a)-(e) illustrate the models used in the present experiments. Each model consisted of a pair



(c) Type C-S model



(d) Type C-SR model



(e) Type C-R model

Fig. 2 Schematic diagrams of the airframe-integrated inlet models.

of side walls, a top wall, and a cowl. The top wall plate simulated the windward surface of the vehicle, and was installed at the mid height of the wind tunnel. The top plate spanned the entire wind tunnel. The frontal area at the inlet entrance, which projected to a plane normal to the top wall surface, was 15 mm \times 12 mm in all models. The side wall had a swept-back angle of 45 degrees. Their overall geometrical contraction ratio, which is the ratio of the cross section at the entrance to that at the exit of the inlet, was 3. Cowl leading edge was located at the end of the convergent section of the inlet except in several cases of Type *C-SR* and Type *C-R* models. Downstream of the convergent section, there was a constant cross-section duct part, which simulated an isolator. In this study, 16 models, each with a different geometry, were tested.

Type *A* models, which corresponded to Type *a* in Fig. 1, had a flat top wall with inclination angles of 0, 3, or 6 degrees. These three angles were employed to evaluate the quantitative tendency of the inlet performance. Each configuration was designated by combining an inclination angle and the model type, such as *A-3* (Fig. 2 (a)). The inlet employed only side-wall compression.

The top plate of Type *B* models had a wedge at its leading edge, which simulated the ramp. The model was attached to the downstream of the ramp, where the surface was parallel to the wind tunnel axis. These models corresponded to Type *b* in Fig. 1. The ramp angle was 3 or 6 degrees. Side walls were the same as those of *A*, and the entrance of the inlet models was located 2 mm downstream or 60 mm downstream of the end of the ramp (indicated by *U* and *D*, respectively). Each model was termed by the model type and the ramp angle followed by *U* or *D*, e.g., *B-3D*. In the *B-3D* and *B-6D* models, the cowl leading edge was located sufficiently downstream so as not to inhale the expansion fan from the corner of the top wall ramp end. In the *B-3U* and *B-6U* models, part of the expansion fan went inside the inlet. By comparing these four Type *B* models, the effect of expansion-fan inhalation on the inlet performance was investigated, as well as the effect of the ramp angle.

In Type *C* models, the top wall had a ramp followed by the parallel surface. The turning angle was 6 degrees. Since the models straddled over the

ramp and the parallel surface, the airflow was turned by the shock wave from the leading edge of the cowl and the expansion fan from the corner of the ramp. The models corresponded to Type *c* in Fig. 1. In this type, with the same geometrical contraction ratio of 3, three models were prepared to compare the ways of compression process: Type *C-S* model employing only side-wall compression, Type *C-SR* model employing both side-wall compression with a contraction ratio of 1.5 and ramp compression with a contraction ratio of 2, and Type *C-R* model employing only ramp compression (Figs. 2 (c)-(e)). The top walls of the *C-SR* and *C-R* models had a 6-degree second ramp inside the inlet, which started at the leading edge of the inlet. Four cowls with different lengths were prepared for the *C-SR* and *C-R* models to reduce extra spillage caused by the shock wave from the second ramp. These cowls were referred by the designations *S*, *M-1*, *M-2* and *L*, and their lengths are shown in Figs. 2 (d) and (e).

(C) Instrumentation

Twenty-two to twenty-eight pressure holes were bored on the centerline of the top wall. 2 to 8 on the side walls, and 3 on the centerline of the cowl were also tapped. The diameter of each hole was 0.7 mm. In the constant-cross-section duct part, i.e., the isolator, pitot pressures were measured at 5 to 12 points in a cross section. The inner and the outer diameters of the pitot tube were 0.3 mm and 0.6 mm, respectively. The one to four pitot tubes were used at a test for ensuring the airflow path in the models. The wall pressure with the pitot tubes was assured to be the same as that with no pitot tube. Wall pressure was measured with a 50 psia pressure transducer, and the pitot pressure was with 200 psia. Accuracy of the wall-pressure measurement system was $\pm 0.5\%$. Because of the difficulty of determining the flow direction inside the models, the flow static pressure was linearly interpolated from the wall pressures on both sides at the same lateral location. With this interpolated pressure and the measured pitot pressure, the local flow properties, e.g., total pressure, were evaluated.

During the wind tunnel operation, the shadow-graph image of the flow field outside the inlet was observed for all the models with a CCD video camera. It was confirmed that the shock wave from the top-wall leading edge did not interact with the flow field

around the inlet models.

Experimental results and discussion

Figures 3 (a)-(f) show the wall pressure distributions on the centerline of the top-wall. In Figs. 3 (e) and (f), the effect of the cowl length is shown. Figures 4 (a)-(p) show the oil flow patterns. Table 1 summarizes the experimental results of the mass capture ratio (CR), the total pressure efficiency (η_{pt}), kinetic energy efficiency (η_{KE}), and the area-averaged Mach number in the isolator. In this table, the subscripts 'total' and 'inlet' indicate inclusion and exclusion of the pre-compression effect by the top wall, respectively. The definitions of the coefficients and others are as follows:

$$CR_{total} = \frac{\int \rho_2 u_2 dA}{\int \rho_{ref} u_{ref} dA} = \frac{(\text{air mass flow rate in the isolator})}{(\text{air mass flow at the reference condition})} \quad (1)$$

$$CR_{inlet} = \frac{\int \rho_2 u_2 dA}{\int \rho_1 u_1 dA} = \frac{(\text{air mass flow rate in the isolator})}{(\text{air mass flow rate at the entrance of the model})} \quad (2)$$

$$\eta_{pt, total} = \frac{\int P_{t,2} \rho_2 u_2 dA / \int \rho_2 u_2 dA}{\int P_{t,ref} \rho_{ref} u_{ref} dA / \int \rho_{ref} u_{ref} dA} = \frac{(\text{mean total pressure weighted by mass flow rate in the isolator})}{(\text{total pressure weighted by mass flow rate at the reference condition})} \quad (3)$$

$$\eta_{pt, inlet} = \frac{\int P_{t,2} \rho_2 u_2 dA / \int \rho_2 u_2 dA}{\int P_{t,1} \rho_1 u_1 dA / \int \rho_1 u_1 dA} = \frac{(\text{mean total pressure weighted by mass flow rate in the isolator})}{(\text{mean total pressure weighted by mass flow at the entrance of the model})} \quad (4)$$

The properties at the reference condition were substituted by those obtained at the entrance of the Type A-0 model, i.e., the averaged values of 15 mm × 12 mm area at the inlet entrance, including the boundary layer on the plate. ξ is the ratio of the area-weighted average of the top-wall pressure in the isolator to the free-stream static pressure. This represents a mean pressure ratio of the inlet model. Here, the characteristics of each model are discussed.

(A) Type A models

According to Figs. 4 (a)-(c), the impingement of

the shock wave from the leading edge of the side wall appeared only at the cowl side on the side wall, which was approximately half of the height of the side wall in the three models. As the inclination angle increased, the shock angle from the leading edge of the cowl increased. The entrance Mach number decreased with the inclination angle.

CR_{total} and ξ were improved as the inclination angle increased (see Table 1 and Fig. 3(a)). CR_{inlet} became slightly lower because of the reduction of the entrance Mach number by the stronger shock wave from the leading edge of the top wall. With reduction of the Mach number, spillage from the open-bottom increased due to the effect of the swept-back geometry.²⁾ $\eta_{pt, total}$ also showed a slight increase with the larger inclination angle. The increase of the top wall angle diminished the top-wall boundary layer thickness. The measured heights of the boundary layer of 99% primary flow velocity at the inlet entrance of the A-0, A-3, A-6 models were 4.2 mm, 3.8 mm, and 2.8 mm, respectively. The reduction of the fraction of the boundary layer to the entire flow captured by the inlet resulted in better total pressure efficiency. The kinetic energy efficiency was evaluated from the experiments and no substantial difference was found between the models.

From the viewpoint of the advantage of pre-compression and the mass capture, the inlet should be installed on the ramp portion of the airframe windward surface. The larger inclination angle of the top-wall plate resulted in better performances within the range of the present experimental conditions.

(B) Type B models

These models virtually canceled out the pre-compression effect. The oil flow patterns of the B-3D and B6-D models were similar to that of the A-0 model. However, the corner vortex along the junction of the side wall and the top wall was larger in the B-3U and B-6U models in Figs. 4 (d) and (e), which was due to the expansion at the ramp corner. In spite of the existence of a ramp of 3 or 6 degrees, both CR_{total} and $\eta_{pt, total}$ were almost equal to those of the A-0 model. The pressure ratio also became compatible with the A-0 model. The relative position of the inlet to the ramp corner did not result in a significant change in the performance. Thus, in the simulation for Type b, the airflow was assumed to enter the inlet

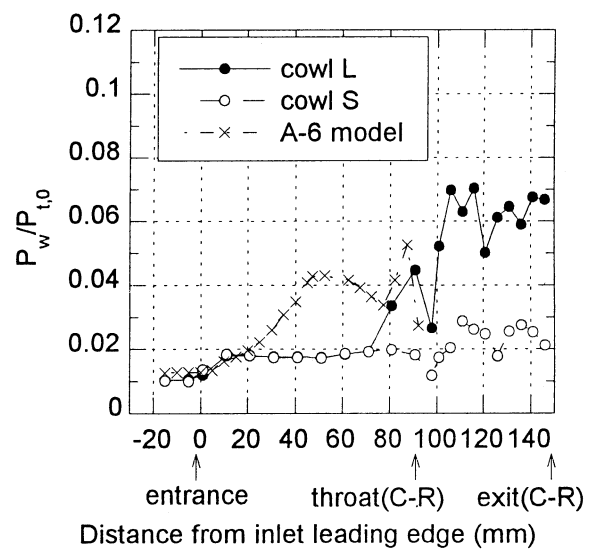
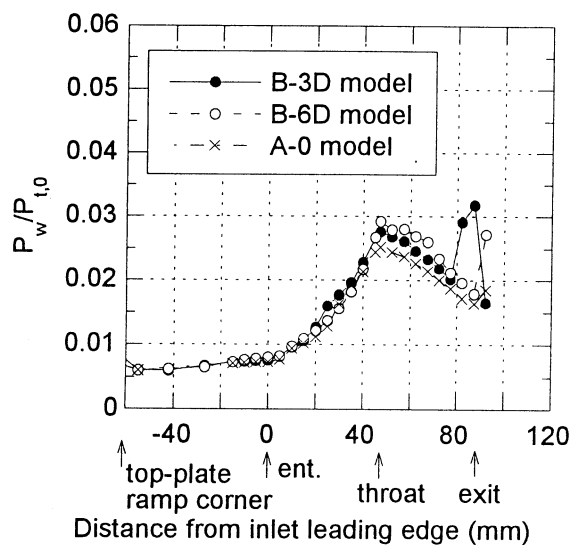
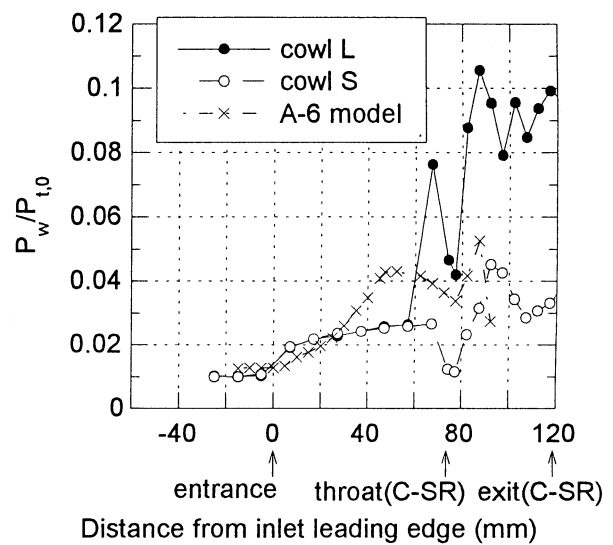
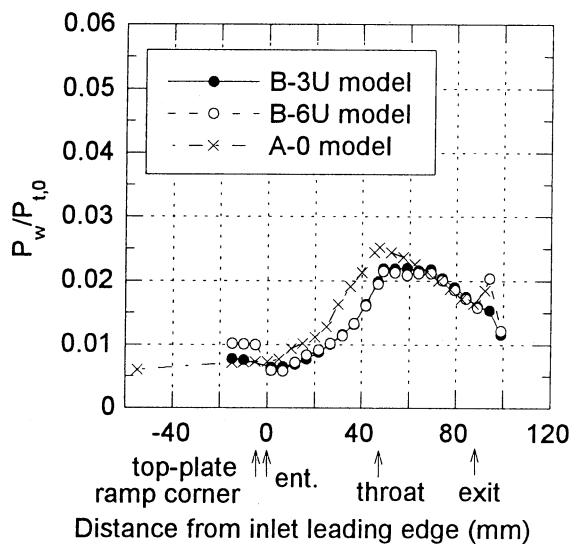
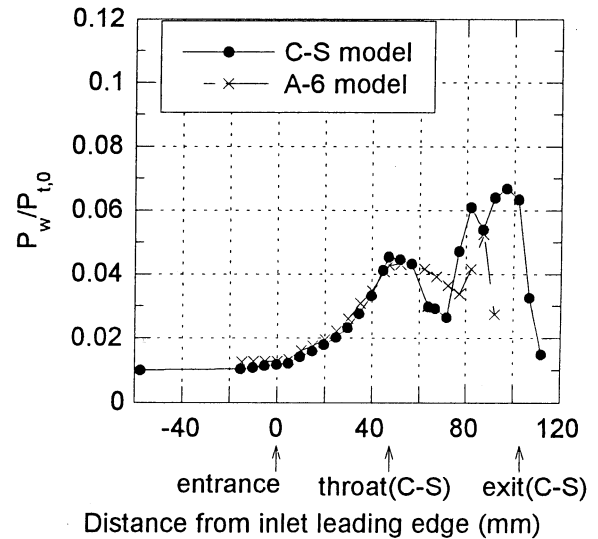
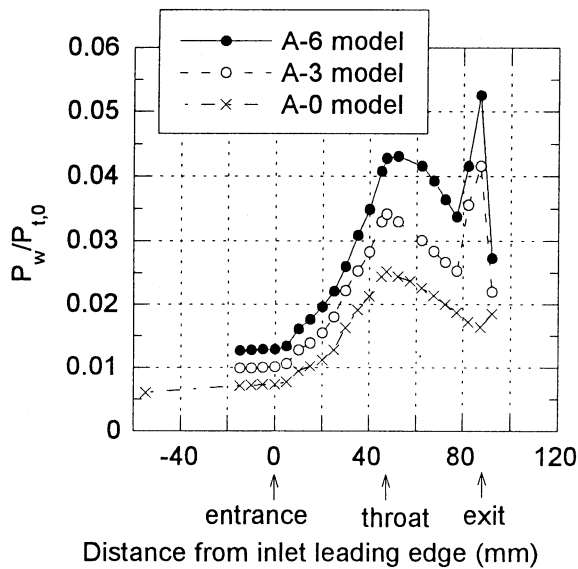
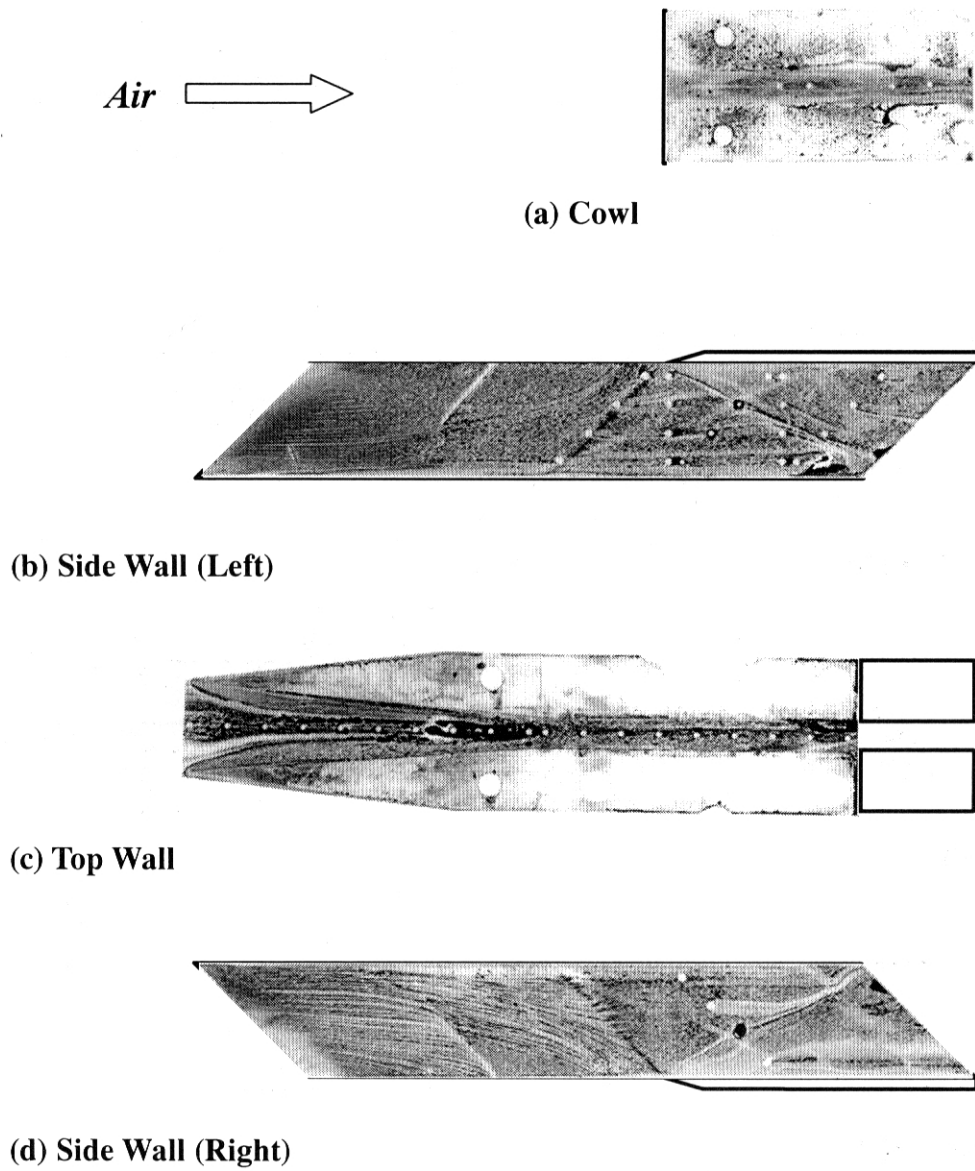


Fig. 3 Wall pressure distributions on the centerline of the top wall.

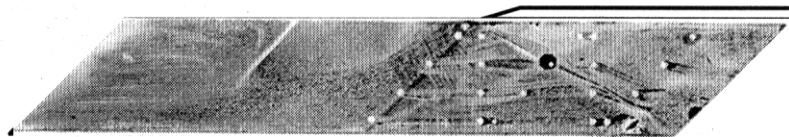


(a) Type A-0 model

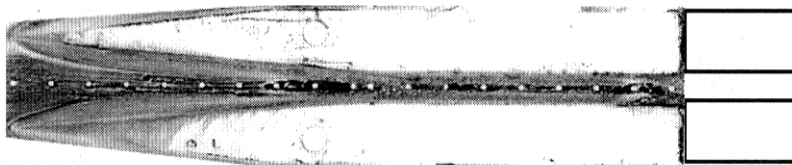
Fig. 4 Oil flow patterns



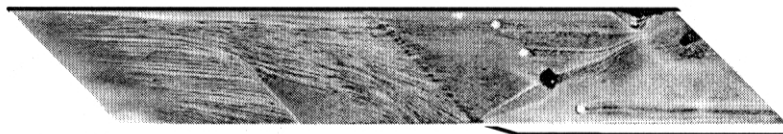
(a) Cowl



(b) Side Wall (Left)



(c) Top Wall



(d) Side Wall (Right)

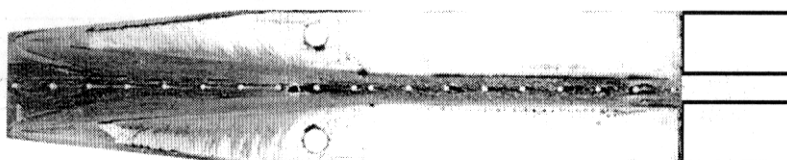
(b) Type A-3 model



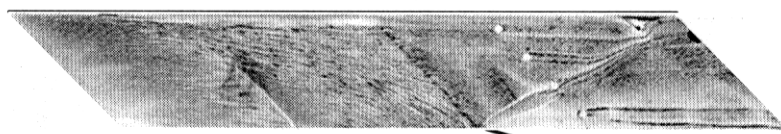
(a) Cowl



(b) Side Wall (Left)



(c) Top Wall

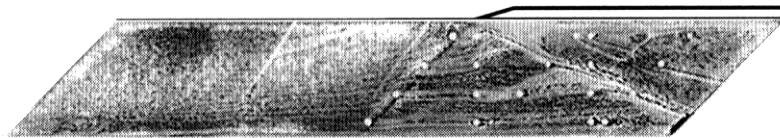


(d) Side Wall (Right)

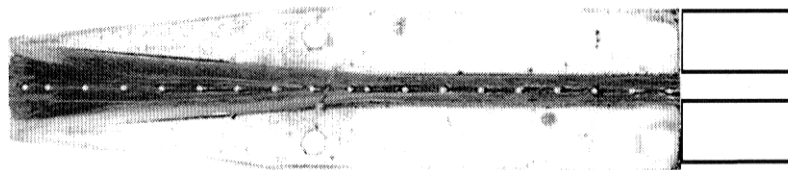
(c) Type A-6 model



(a) Cowl



(b) Side Wall (Left)



(c) Top Wall



(d) Side Wall (Right)

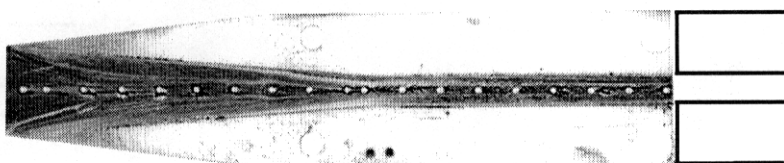
(d) Type B-3U model



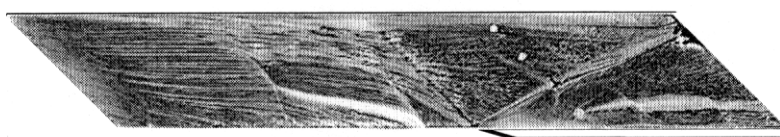
(a) Cowl



(b) Side Wall (Left)



(c) Top Wall



(d) Side Wall (Right)

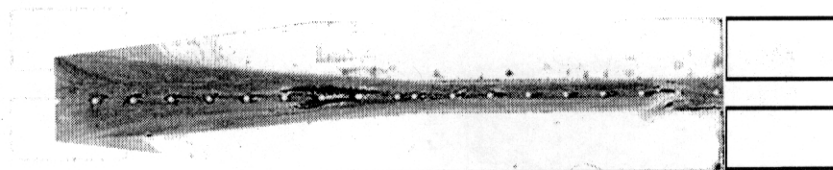
(e) Type B-6U model



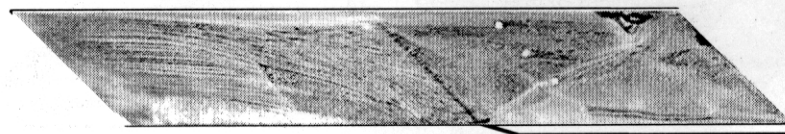
(a) Cowl



(b) Side Wall (Left)



(c) Top Wall



(d) Side Wall (Right)

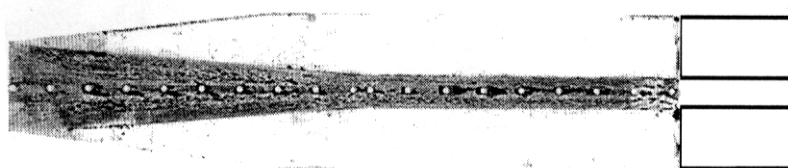
(f) Type B-3D model



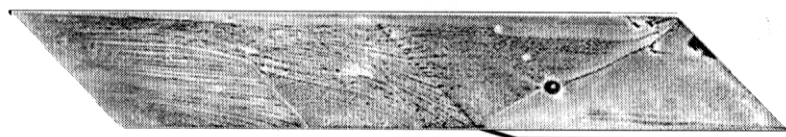
(a) Cowl



(b) Side Wall (Left)

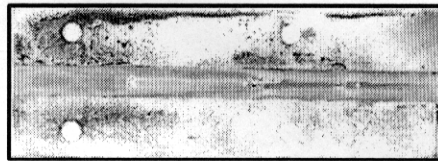
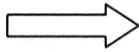
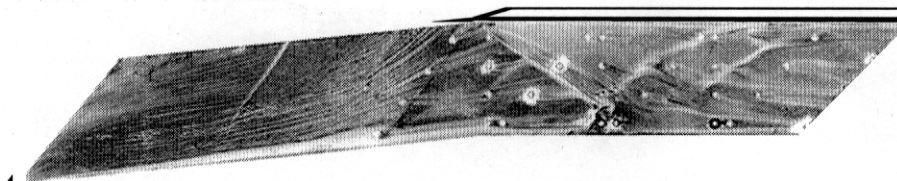
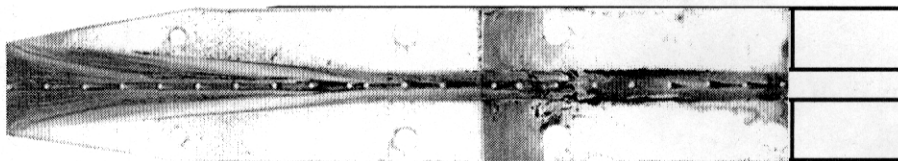
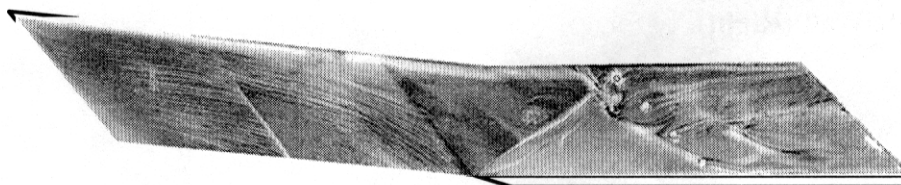


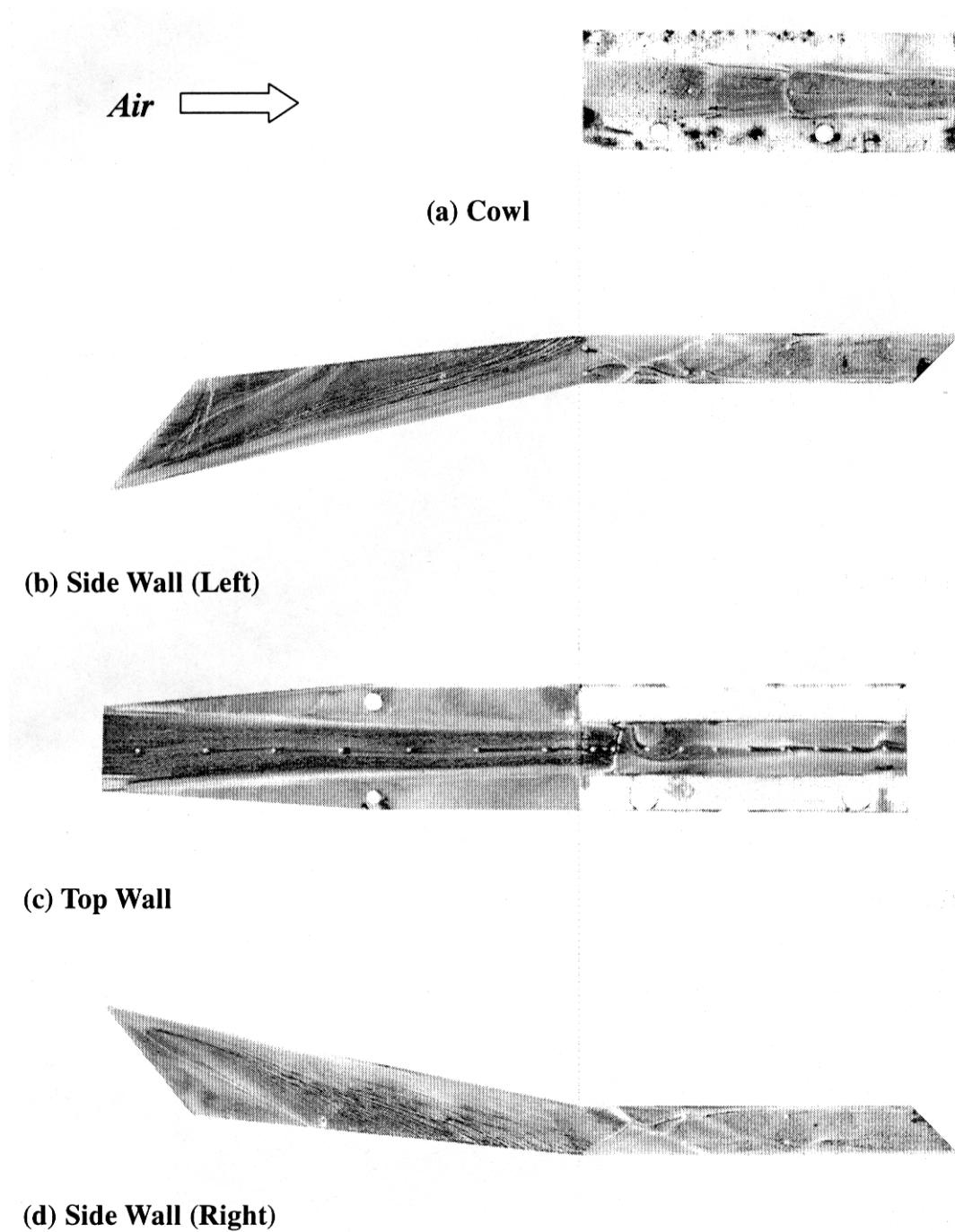
(c) Top Wall



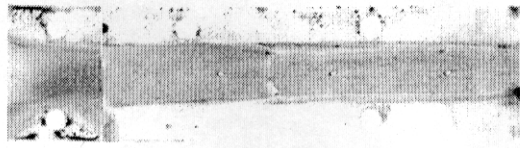
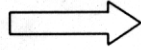
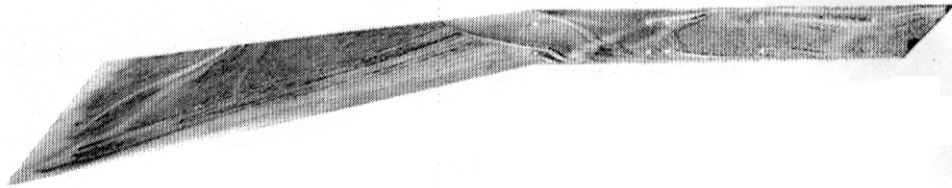
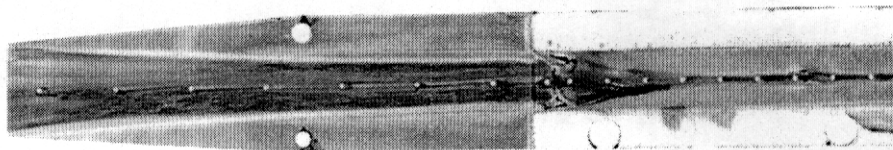
(d) Side Wall (Right)

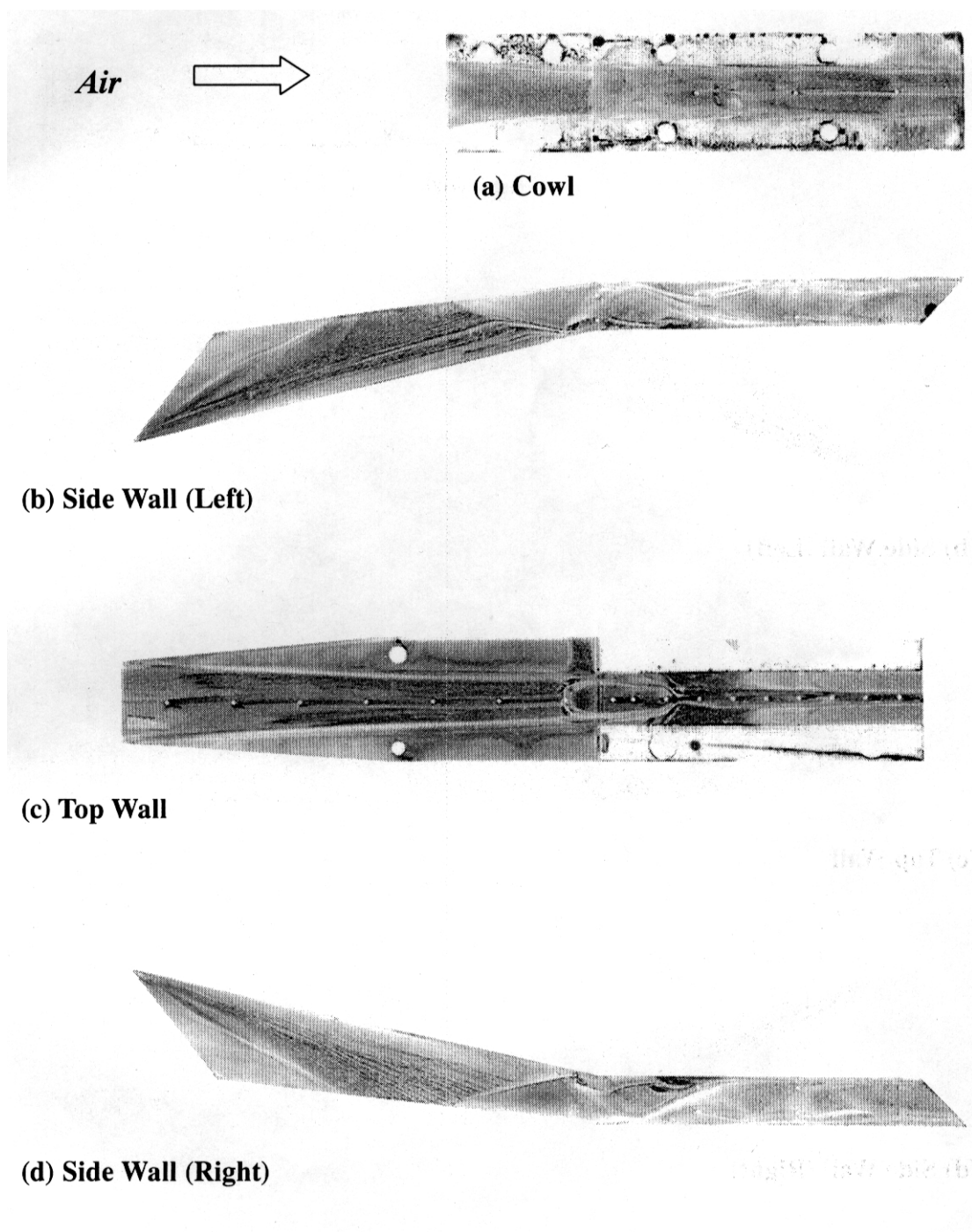
(g) Type B-6D model

Air**(a) Cowl****(b) Side Wall (Left)****(c) Top Wall****(d) Side Wall (Right)****(h) Type C-S model**

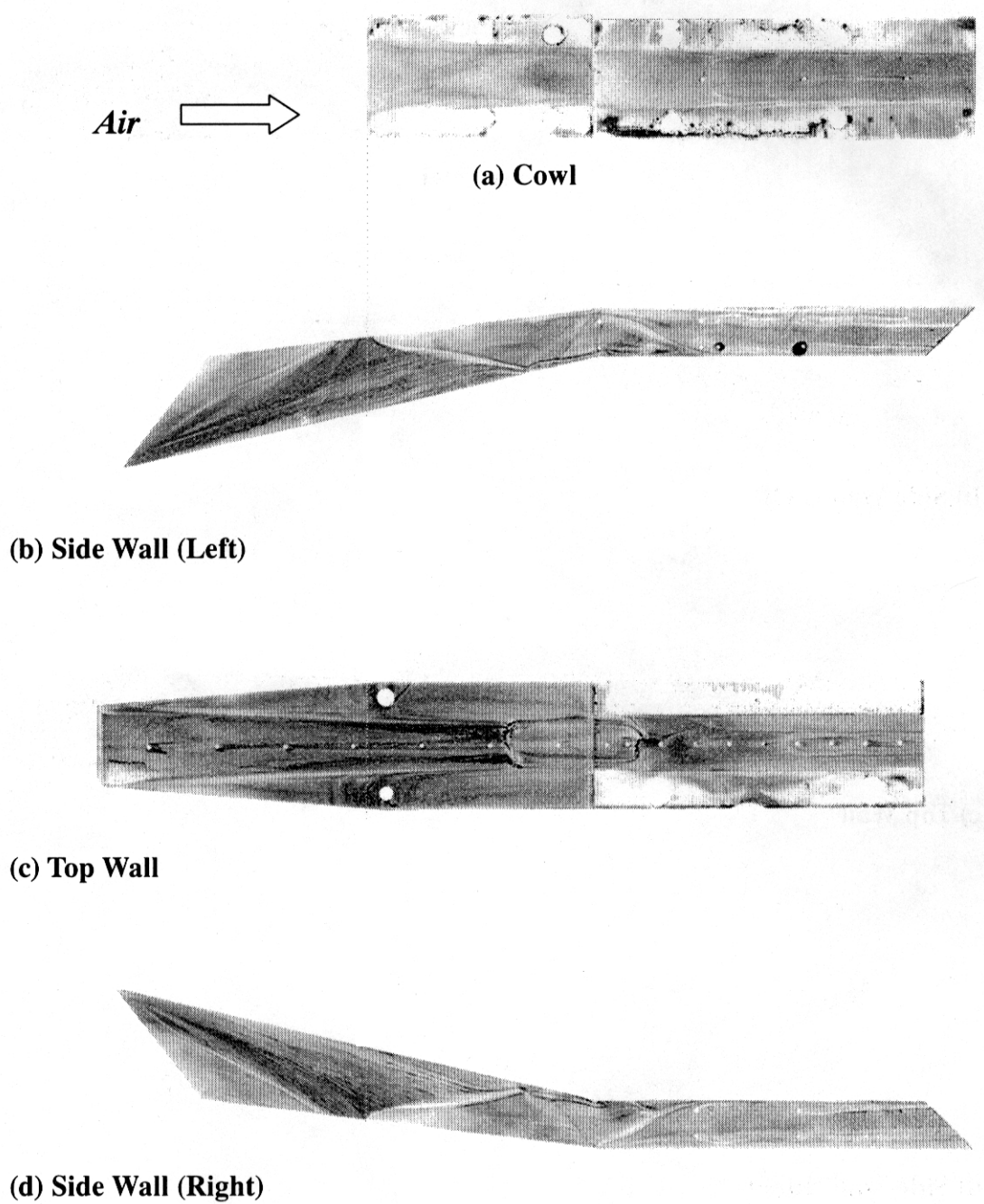


(i) Type C-SR S model

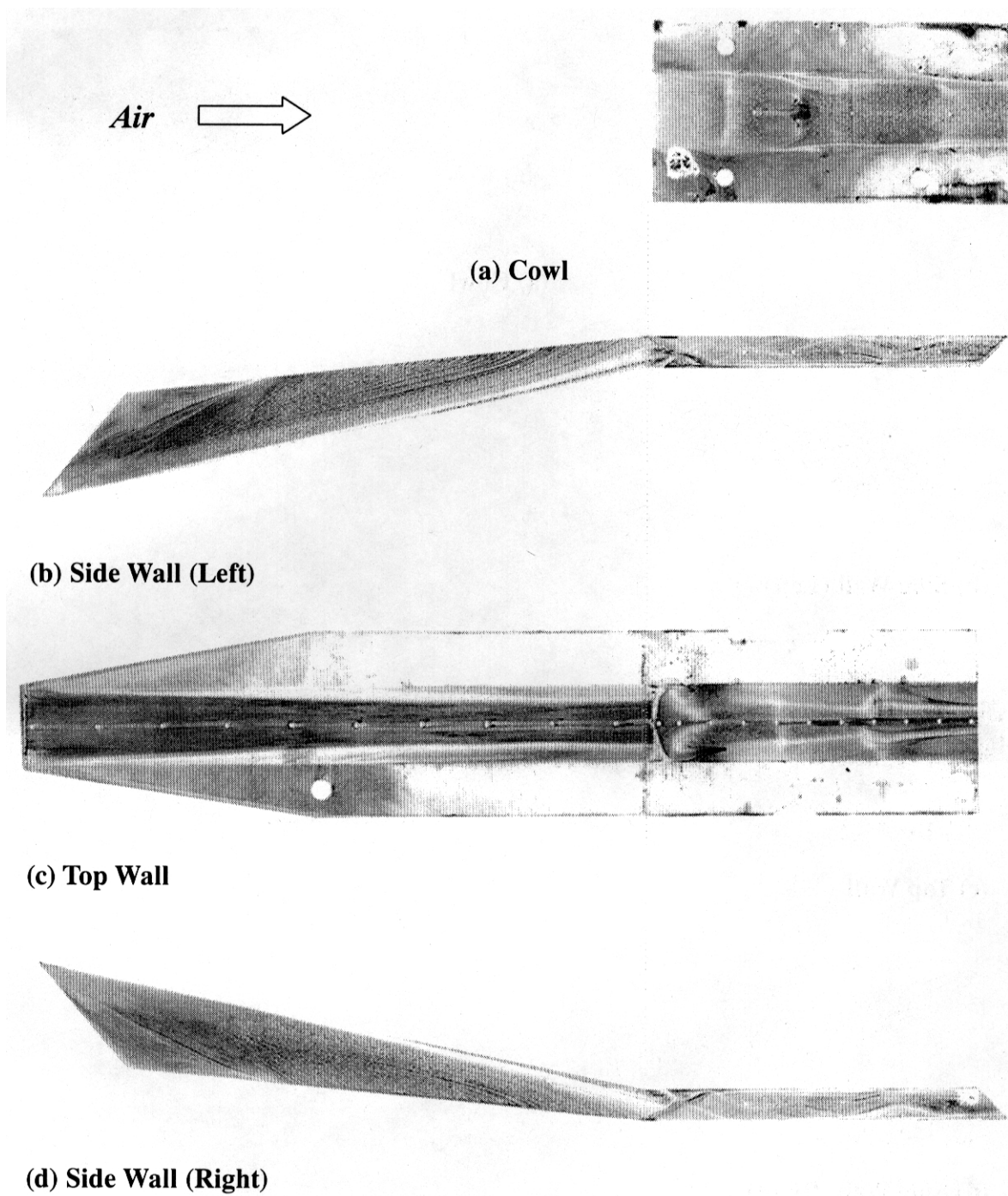
Air**(a) Cowl****(b) Side Wall (Left)****(c) Top Wall****(d) Side Wall (Right)****(j) Type C-SR M1 model**



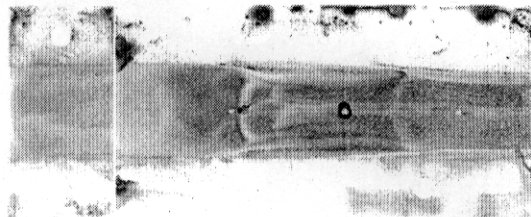
(k) Type C-SR M2 model



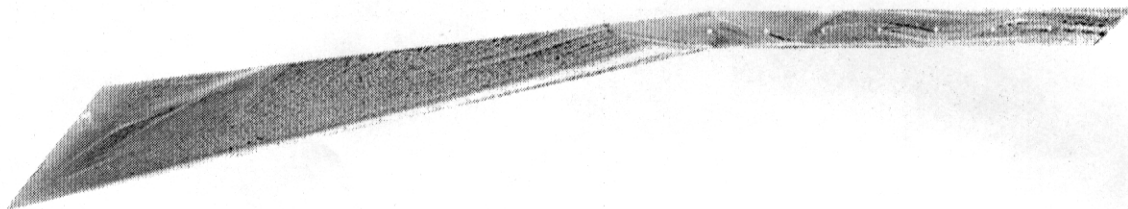
(l) Type C-SR L model



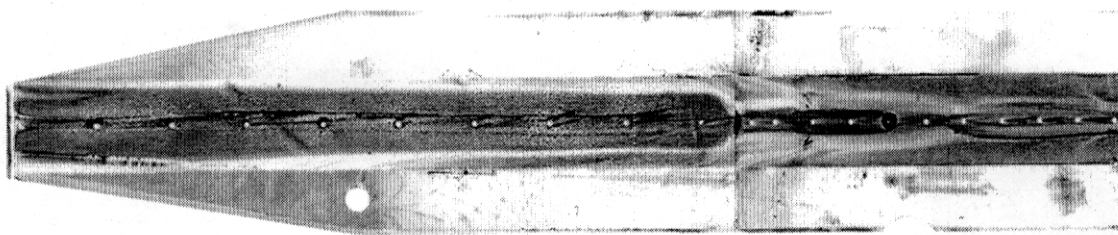
Air →



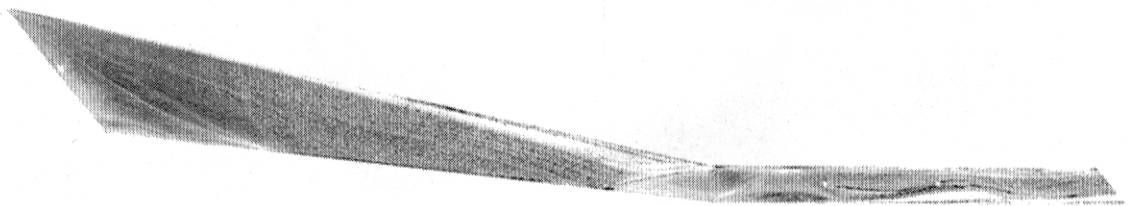
(a) Cowl



(b) Side Wall (Left)

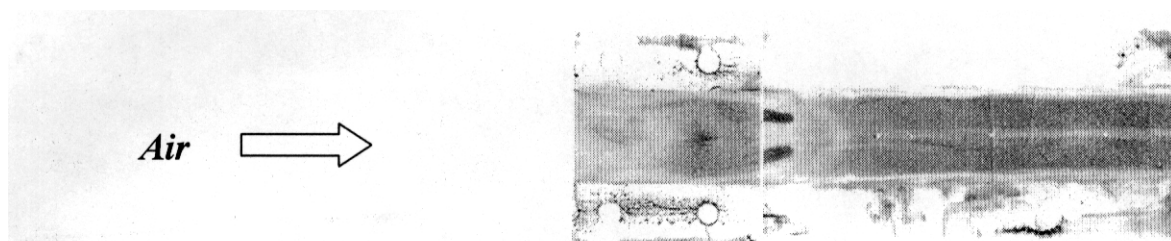


(c) Top Wall

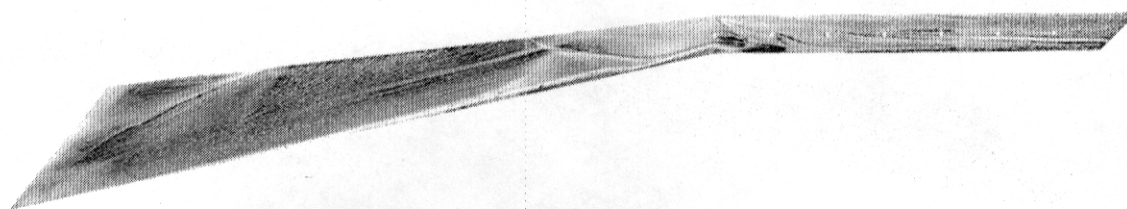


(d) Side Wall (Right)

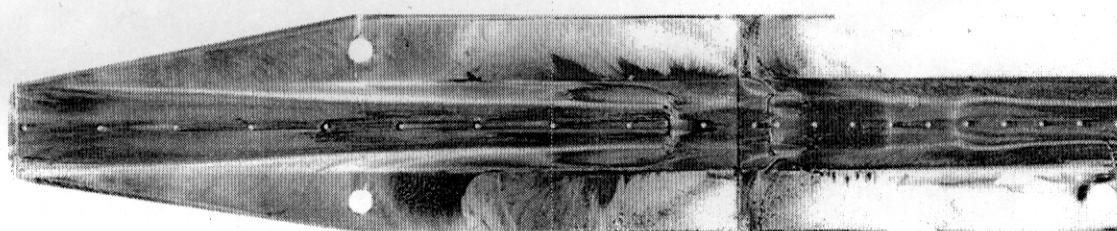
(n) Type C-R M1 model



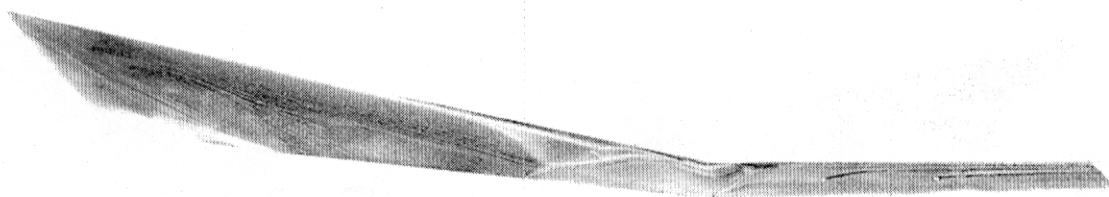
(a) Cowl



(b) Side Wall (Left)



(c) Top Wall



(d) Side Wall (Right)

(e) Type C-R M2 model

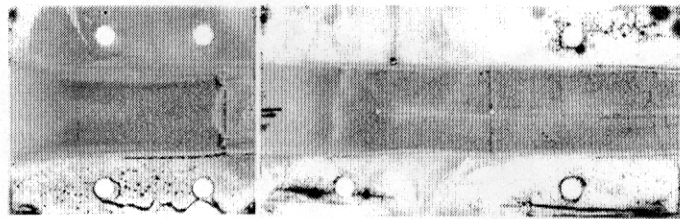
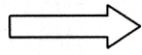
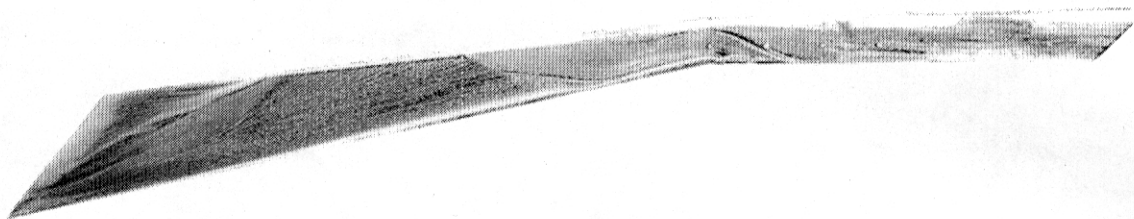
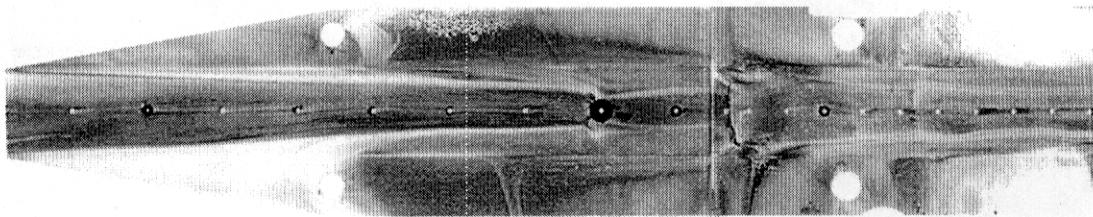
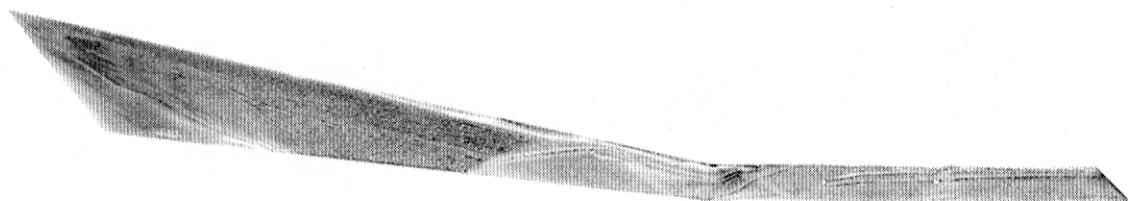
Air**(a) Cowl****(b) Side Wall (Left)****(c) Top Wall****(d) Side Wall (Right)****(p) Type C-R L model**

Table 1 Performance of inlet models

	M_2	$\rho_2 u_2$	CR_{inlet}	CR_{total}	$\eta_{Pt\ inlet}$	$\eta_{Pt\ total}$	$\eta_{KE\ inlet}$	ξ
A-0	2.48	862.2	0.674	0.674	0.591	0.591	0.953	3.9
A-3	2.28	1064.5	0.676	0.832	0.613	0.611	0.951	5.6
A-6	2.13	1240.8	0.613	0.970	0.639	0.626	0.950	7.3
B-3D	2.38	897.3	0.714	0.701	0.626	0.624	0.958	4.7
B-6D	2.53	964.3	0.792	0.754	0.585	0.572	0.952	4.4
B-3U	2.66	891.2	–	0.696	0.593	0.591	0.953	3.6
B-6U	2.55	813.3	–	0.636	0.561	0.550	0.948	3.6
C-S	1.90	1232.7	0.610	0.963	0.430	0.421	0.900	8.7
C-SR S	2.40	1081	0.535	0.845	0.666	0.652	0.955	5.3
C-SR M1	2.16	1461.9	0.723	1.142	0.601	0.589	0.943	8.4
C-SR M2	1.94	1567.8	0.775	1.225	0.542	0.531	0.930	11.4
C-SR L	1.63	1866.6	0.923	1.459	0.537	0.525	0.929	15.1
C-R S	2.24	662	0.327	0.517	0.273	0.267	0.836	4.1
C-R M1	2.37	1164	0.576	0.910	0.539	0.528	0.929	6.4
C-R M2	1.92	1188	0.588	0.928	0.363	0.355	0.877	9.5
C-R L	1.89	1408.1	0.696	1.100	0.450	0.441	0.906	10.8

after it went through the expansion wave completely. This configuration did not get any advantage from the pre-compression.

(C) Type C models

According to oil flow patterns, there was separation on the top wall downstream of the corner of the ramp. When the shock wave from the leading edge of the cowl impinged on the ramp, there was separation downstream of the impingement. They are common features of the Type C models.

This configuration attained sufficient mass capture. CR_{total} of the Type C-S model was as high as that of the A-6 model, and ξ was better than that of the A-6 model. On the other hand, $\eta_{Pt, total}$ became lower than that of the A-6 model. In the Type C-SR model, ξ and CR_{total} became higher as the cowl was extended upstream. These values were equal to or greater than those of the A-6 model, when the cowl was extended sufficiently. The cowl extension caused no significant reduction in $\eta_{Pt, total}$. In Type C-R model, with the extended cowl, CR_{total} was as high as that of the A-6 model and ξ increased. On the other hand, $\eta_{Pt, total}$ of the C-R_S model became significantly lower than that of the A-6 model caused by larger spillage of the primary flow.

The pre-compression effect was attained in the Type A and Type C models. In the Type B models, the pre-compression effect was lost. In the Type B

models, there was no difference in the inlet performances by their relative positions. Although the models showed different characteristics of the performance, most of the Type A, Type B and Type C-SR models showed the similar values in $\eta_{KE, inlet}$ and CR_{inlet} .

The swept angles of the models were the same of 45 degrees in the tests. The decrease of the swept angle of the side walls does not improve the air capture greatly when the entrance Mach number is high, e.g., Mach 6 or more, and the reflections of the shock waves are few times, e.g., once or twice. The low air capture of the Type B model cannot be improved fundamentally by the decrease of the swept angle. The experimental result indicated that the pre-compression effect was lost in the Type b integration configuration.

SIMULATIONS OF SCRAMJET ENGINE AND FLIGHT OF THE SSTD AEROSPACE PLANE

In this chapter, based on the experimental results, difference in the scramjet engine performance and the difference in payload of the aerospace plane due to the engine-airframe integration form are examined. In the actual flight, several types of engines or engine-modes are used to match the velocity region. However, in this study, the effect of the engine-airframe integration is considered only in the scramjet-

operating regime, where the pre-compression affects the engine performance significantly.

Integration of scramjet engine into airframe

Three airframe integration configurations, i.e., Types *a*, *b* and *c*, were examined (Fig. 1). All the airframes had a two-dimensional sharp-wedge nose, and their length, width and the windward surface wedge angle from the airframe axis were 80m, 15m, and 3 degrees, respectively. The angle of the external nozzle was different in each model.

In Type *a*, the shock from the forebody nose impinged on the leading edge of the cowl at the flight Mach number of 12. In Type *b*, the upstream part of the forebody was the same as that of Type *a*, but the ramp was terminated and the vehicle surface was parallel to the airframe axis just upstream of the scramjet engine. As was confirmed by the experiments, it was assumed that the pre-compressed air passed through the entire expansion fan from the corner of the airframe before it entered the engine. In Type *c*, the scramjet engine was aligned with the airframe axis. However, the cowl was extended forward to capture the same mass flow rate as that of Type *a*. The airflow was turned toward the airframe axis by the shock wave from the cowl.

Calculation methods

The estimation of the scramjet engine performance and the simulation of the flight of the space plane were conventional methods. Here, the inlet performances were different due to the integration type of the inlet to the airframe. The other scramjet components had the same performances in the simulation.

(A) Scramjet engine performance

The scramjet engine performance was calculated with the quasi-one-dimensional flow method. The air entering the engine passed a planar shock wave generated by the forebody, which was calculated with the 2D oblique shock wave relations. The end effect at both sides of the forebody¹⁶⁾ was neglected for the sake of simplicity. In the calculation of the engine performance, the angle of attack, i.e., the angle between the free-stream direction and airframe axis, was fixed to be 3 degrees.

The airflow condition into the inlet was calculated

for each integration type, and CR_{inlet} was assumed to be 1.0, i.e., no spillage from the inlet. The effect of the boundary layer on the airframe surface on engine performance was not considered. The inlet performances were calculated with $\eta_{KE,inlet}$ of 0.98, which was deduced from an empirical equation.¹⁷⁾ According to the experiments, there was no significant difference in $\eta_{KE,inlet}$ between the three types of the inlet models. The geometrical contraction ratio was 5. From Mach 6 to 8, the amount of the fuel was adjusted so that the Mach number of the combustion gas in the constant cross section duct was just above unity to avoid thermal choking. From flight Mach numbers 8 to 12, the stoichiometric hydrogen fuel was vertically injected in the constant cross section duct and the fuel reacted completely. In the internal nozzle, the combustion gas expanded isentropically and one-dimensionally with an expansion area ratio of 5. In the external nozzle, the combustion gas expanded through a two-dimensional expansion wave.

Both air and the combustion gas were calorically and thermally ideal. The ratios of the specific heats were 1.40 for air and 1.25 for the combustion gas, respectively, and the molecular weight of the combustion gas was 24.7. These properties of the combustion gas were calculated with a code¹⁸⁾ in the equilibrium condition. The heat release at combustion by hydrogen was 121×10^3 kJ per 1 kg hydrogen.

The engine internal thrust was calculated as follows. First, the difference of the impulse-functions between the inlet entrance and the internal nozzle exit was calculated. This was designated as the inviscid thrust. Then the friction drag of the internal surface was estimated and was subtracted from the inviscid thrust to obtain the internal thrust. The total thrust was defined as the sum of the engine internal thrust and force/drag on the windward airframe surface, including forebody, aft-body and cowl of the engine module. The friction coefficient was set to be 0.0025 on the entire surface.¹⁹⁾

(B) Payload estimation

The effect of the airframe-scramjet integration on payload was estimated by a flight simulation of a SSTO aerospace plane to a 100-km low earth orbit. The aerodynamic data of the plane, the other engine performances and the weights of the vehicle components were the same as those used in a previous

investigation.²⁰⁾ The gross take-off mass was 460 Mg.

From take-off to Mach 6, the air-turbo-ramjet (ATR) operated. The projected cross section of the ATR modules was 15 m^2 at the entrance. The equivalence ratio of the ATR was unity. The specific impulse of the ATR calculated by Sakata, et al.²¹⁾ was used. The scramjet operated from Mach 6 to Mach 12. The projected cross section of the scramjet was 30 m^2 . After operation of the scramjet, the rocket engine took over to carry the vehicle into orbit. The maximum total thrust of the rocket engine was 4060kN, and the specific impulse was $4018 \text{ m}\cdot\text{s}^{-1}$ at the sea level. Propellants were hydrogen and oxygen. The trajectory of the aerospace plane was within the 2-D plane.

Results of the simulation and discussion

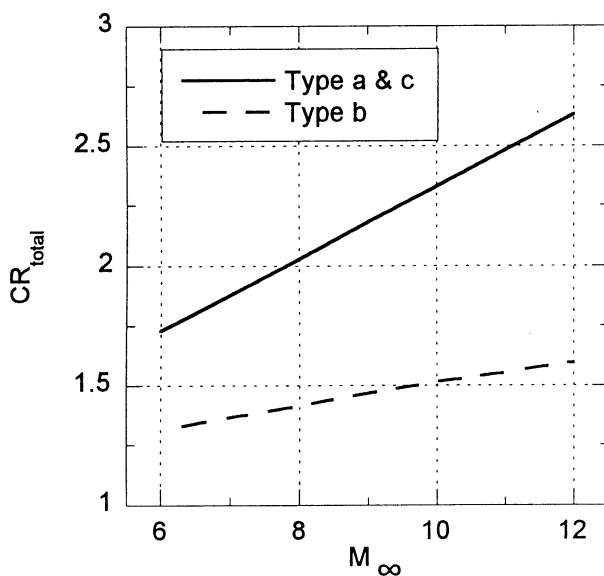
(A) Scramjet engine performance

The calculated performances of the three types of airframe-integrated scramjet engines are shown in Figs. 5 and 6. Figure 5(a) shows the air mass flow into the engine, being non-dimensionalized by the product of the mass flux of the free stream and the projected cross-sectional area at the engine entrance. In all the models, the mass flow rates were larger than unity due to the pre-compression by the angle of attack. In Types *a* and *c*, this was also by the airframe ramp. The mass flow rate of Type *b* was smaller than

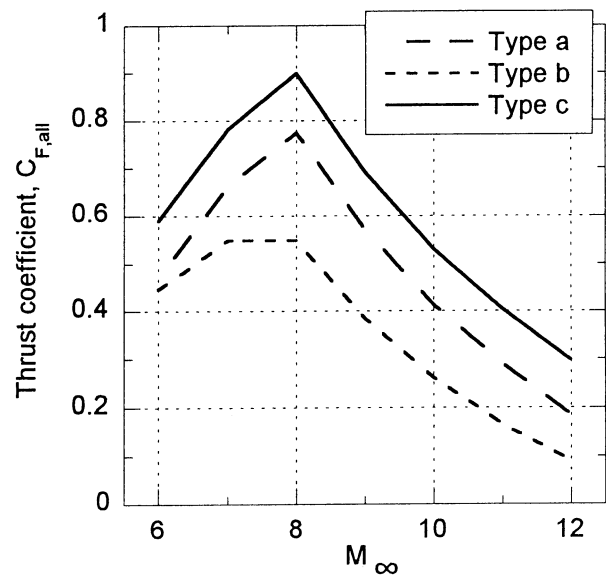
those of Types *a* and *c*. The mass flux of Type *b* decreased due to the expansion fan in front of the engine. The mass capture was about 80% that of Type *a* or Type *c* at Mach 4. In the experiments with the same inlet model, CR_{total} of the Type *B* was about 0.7, and that of the Type A-6 was 0.970. The ratio obtained experimentally showed reasonably good agreement with the calculated one.

Figure 5(b) shows the thrust coefficient of the engine, defined as the ratio of the total thrust to the product of the flight dynamic pressure and the projected cross-sectional area of the engine entrance. Type *c* delivered the largest total thrust and Type *a* was the second largest. Suffering from its smaller air mass flow rate, Type *b* had a significantly lower thrust coefficient than the others. The specific impulses of the engines were not significantly different between Types *a*, *b* and *c*, because there was no difference in the total enthalpy of the unit mass of the combustion gas in the stoichiometric condition. The primary reason in the engine thrust difference was the difference of the air mass flow or the air impulse function into the engine, as was observed in the experiments. The difference in the thrust coefficients became larger in the high Mach number regime, where the difference of the mass capture ratios increased.

Beside the decrease of the air mass flow into the engine, the decrease of the thrust was also caused by



(a) Mass capture ratio



(b) Thrust coefficient with the engine thrust and the drag of the windward surface of the airframe

Fig. 5 Calculation results.

inadequacy in the airframe and the engine configurations. Figure 6 shows a break-down of the thrust coefficients at the flight Mach number of 10. The difference in the thrust coefficient between Type *a* and Type *c* was due to the differences in the external nozzle thrust and the cowl drag in addition to the engine internal thrust. As for the internal thrust, Type *a* had a disadvantage since the direction of engine thrust was not aligned to the airframe axis.

As shown in Fig. 1, the divergence angle of the external nozzle of Type *a* was larger than that of Type *c*. The further expansion of the combustion gas in the external nozzle of Type *a* resulted in lower wall pressure and smaller thrust than that of Type *c*, even though the projected area of the external nozzle

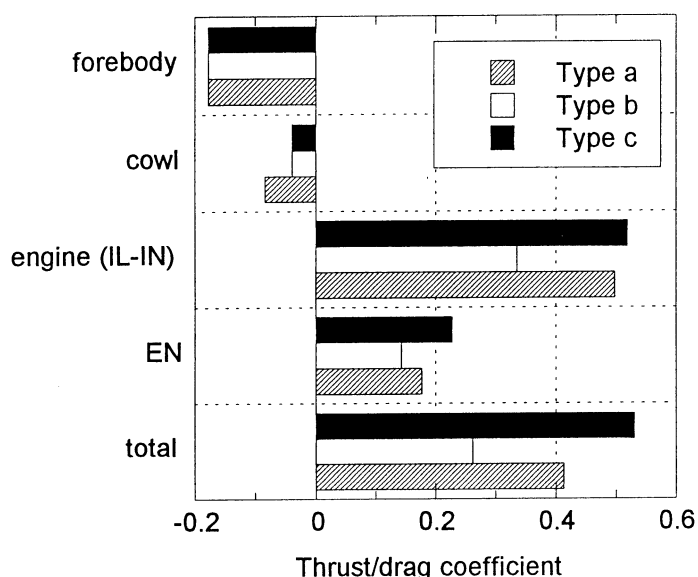


Fig. 6 Breakdown of the thrust coefficients at the flight Mach number of 10.

became larger than that of Type *c*. The cowl drag of Type *b* or Type *c* was smaller than that of Type *a*, since the cowl outer surface is parallel to the airframe axis and thus the pressure drag was small.

(B) Payload estimation of the SSTD aerospace plane

Table 2 lists the contents of the mass of the aerospace plane in the payload estimation. The payload of Type *a* was 5.9Mg, whereas that of Type *c* was 19.0Mg. The operating time and the consumed fuel of Type *a* were larger than those of Type *c* because of the lower thrust. The difference in the engine and the airframe configurations caused the large difference in the payload.

Type *b* could not produce sufficient thrust during the scramjet engine operation, and thus the calculated payload became negative. The engine inhaled a smaller amount of air flow and delivered lower thrust than the other types due to the inadequacy of the integration form of the engine into the airframe. Type *b* configuration should be avoided.

As a result, the inlet should be installed on the ramp to inhale the pre-compressed air, but the section downstream of the inlet entrance should be turned parallel to the airframe axis to reduce the cowl drag and to increase the thrust at the external nozzle.

CONCLUSIONS

The effects of the configuration of the scramjet integration into the airframe on the engine performance and the payload were investigated. The inlet performances were experimentally studied in several configurations, and the effect of the integration forms on the scramjet performance and the payload of the

Table 2 Contents of mass of aerospace plane (unit: Mg)

Item	Model		
	Type <i>a</i>	Type <i>b</i>	Type <i>c</i>
Propellant			
Fuel (ATR)	40.5	40.5	40.5
Fuel (Scramjet)	86.1	100.4	54.4
Fuel (Rocket)	30.8	29.5	33.9
Oxygen	184.9	177.1	203.2
Total propellants	342.3	347.5	332.0
Tank			
Hydrogen	17.6	19.0	14.5
Oxygen	3.1	3.0	3.4
Total tanks	20.7	22.0	17.9
Airframe and engines	91.1	91.1	91.1
Payload	5.9	-0.6	19.0
Total initial mass	460.0	460.0	460.0

SSTO plane were calculated using simple models. The investigation clarified the following points.

(1) When the inlet was integrated on the ramp surface of the airframe, as in the Type A model, a larger ramp angle resulted in better performances in mass capture ratio and pressure ratio within the conditions tested. However, the pressure drag on the cowl increased and the thrust at the external nozzle decreased. Thus, the payload decreased.

(2) When the inlet was attached to the airframe surface parallel to the axis, as in the Type B model, the pre-compression effect was neutralized. The effect of the neutralization was observed even when the inlet model was located just downstream of the ramp corner. The air mass flow into the engine decreased, and the payload was the smallest with Type B configuration.

(3) In the case that the inlet entrance was attached to the airframe ramp surface with subsequent engine components parallel to the airframe axis, as in Type C, the engine showed the best performance. With this configuration, the pre-compressed air was effectively inhaled, cowl drag was reduced, and thrust at the external nozzle was increased. The payload was the largest in the present study.

ACKNOWLEDGMENT

The authors acknowledge the assistance of Yoshinori Futonagane, Yusuke Oikawa, and Tomoyuki Abe, former graduate and under-graduate students of Tohoku University, in conducting the experiments.

REFERENCES

- 1) W.H. Heiser, D.T. Pratt, D.H. Daley and U.B. Mehta; Hypersonic Airbreathing Propulsion, AIAA Education Series (1994) pp. 24-26, AIAA.
- 2) C.A. Trexler and S.W. Sounders; Design and Performance at a Local Mach Number of 6 of an Inlet for an Integrated Scramjet Concept, NASA TN D-7944, (1975/8).
- 3) S. Nomura, K. Hozumi, I. Kawamoto and Y. Miyamoto; Experimental Studies on Aerodynamic Characteristics of SSTO Vehicle at Subsonic to Hypersonic Speeds, Proceedings of the 16th International Symposium on Space Technology and Science, Committee of International Symposium on Space Technology and Science, Tokyo (1988) pp. 1547-1554.
- 4) A.W. Wilhite, W.C. Engelund, D.O. Stanley, J.C. Neftel, R.A. Lepsch, L.B. Bush and K.E. Wurster; Technology and Staging Effects on Two-Stage-to-Orbit Systems, Journal of Spacecraft and Rockets, Vol. 31, No. 1 (1994) pp. 31-38.
- 5) M. Maita, H. Miyajima and T. Mori; System Studies on Space Plane Powered by Scram/LACE Propulsion System, AIAA Paper 92-5024 (1992/12).
- 6) J.J. Bertin, M.C. Towne, M.A. Malan, A.F. Kreins, M.E. Zuber and M.B. Parks; Viscous/Inviscid Interactions of the Forebody Flowfield of an Airbreathing Hypersonic Vehicle, Journal of Spacecraft and Rockets, Vol. 35, No. 4 (1998) pp. 442-449.
- 7) D.C. Freeman, T.A. Talay, D.O. Stanley, R.A. Lepsch and A. W. Wilhite; Design Options for Advanced Manned Launch Systems, Journal of Spacecraft and Rockets, Vol. 32, No. 2 (1995) pp. 241-249.
- 8) J.L. Leingang, L.Q. Maurice and L.R. Carreiro; In-Flight Oxidizer Collection Systems for Airbreathing Space Boosters, Developments in High-Speed-Vehicle propulsion Systems, Progress in Astronautics and Aeronautics (1996) pp. 333-384, AIAA.
- 9) H. Ikawa; Rapid Methodology for Design and Performance Prediction of Integrated Supersonic Combustion Ramjet Engine, Journal of Propulsion and Power, Vol. 7, No. 3, (1991) pp. 437-444.
- 10) W.H. Heiser, D.T. Pratt, D.H. Daley and U.B. Mehta; Hypersonic Airbreathing Propulsion, AIAA Education Series (1994) pp. 198-201, AIAA.
- 11) L.D. Huebner; Computational Inlet-Fairing Effects and Plume Characterization on a Hypersonic Powered Model, Journal of Aircraft, Vol. 32, No. 6 (1995) pp. 1240-1245.
- 12) T.J. Bogar, J.F. Alberico, D.B. Johnson, A.M. Espinosa and M.K. Lockwood; Dual-Fuel Lifting Body Configuration Development, AIAA Paper 96-4592 (1996/11).
- 13) T.M. Berens and N.C. Bissinger; Forebody Precompression Effect and Inlet Entry Condition for Hypersonic Vehicles, Journal of Spacecraft and Rockets, Vol. 35, No. 1 (1998) pp. 30-36.

- 14) H. Ide, J. Armstrong, K.Y. Szema and J. Haney; Hypersonic Vehicle Forebody Design Studies and Aerodynamic Trends, AIAA Paper 89-2182-CP (1989).
- 15) T. Kanda, T. Komuro, G. Masuya, K. Kudo, A. Murakami, K. Tani, Y. Wakamatsu and N. Chinzei; Mach 4 Testing of Scramjet Inlet Models, Journal of Propulsion and Power, Vol. 7, No. 2 (1991) pp.275-280.
- 16) K. Tani, T. Kanda, K. Kudo and D. Akihisa; Effect of Sides-Spillage from Airframe on Scramjet Engine Performance, Journal of Propulsion and Power, Vol. 17, No. 1 (2001) pp. 139-145.
- 17) W.H. Heiser, D.T. Pratt, D.H. Daley and U.B. Mehta; Hypersonic Airbreathing Propulsion, AIAA Education Series (1994) p. 225, AIAA.
- 18) R.A. Svehla and B.J. McBride; FORTRAN IV Computer Program for Calculating of Thermodynamic and Transport Properties of Complex Chemical Systems, NASA TN D-7056 (1973/1).
- 19) J. Swithenbark; Hypersonic Airbreathing Propulsion, Progress in Aeronautical Sciences, Vol. 8 (1967) p. 245, Pergamon Press.
- 20) T. Kanda and K. Kudo; Payload to Low Earth Orbit by Aerospace Plane with Scramjet Engine, Journal of Propulsion and Power, Vol. 13, No. 1 (1996) pp. 164-166.
- 21) K. Sakata, R. Yanagi, S. Shindo, M. Minoda and H. Nouse; Conceptual Study on Air-Breathing Propulsion for Space Plane, Proceedings of the 16th International Symposium on Space Technology and Science, Committee of International Symposium on Space Technology and Science (1988) pp. 107-112.